Journal of Nondestructive Evaluation (2024) 43:1
https://doi.org/10.1007/s10921-023-01010-3

ORIGINAL PAPER

Application of Iterative Elastic SH Reverse Time Migration to Synthetic Ultrasonic Echo Data

Maria Grohmann[1] · Ernst Niederleithinger[1] · Stefan Maack[1] · Stefan Buske[2]

Received: 27 April 2023 / Accepted: 25 September 2023

Abstract
The ultrasonic echo technique is widely used in non-destructive testing (NDT) of concrete objects for thickness measurements, geometry determinations and localization of built-in components. To improve ultrasonic imaging of complex concrete structures, we transferred a seismic imaging technique, the Reverse Time Migration (RTM), to NDT in civil engineering. RTM, in contrast to the conventionally used synthetic aperture focusing technique (SAFT) algorithms, considers all wavefield types and thus, can handle complex wave propagations in any direction with no limit on velocity variations and reflector dip. In this paper, we focused on the development, application and evaluation of a two-dimensional elastic RTM algorithm considering horizontally polarized shear (SH) waves only. We applied the elastic SH RTM routine to synthetic ultrasonic echo SH-wave data generated with a concrete model incorporating several steps and circular cavities. As these features can often be found in real-world NDT use cases, their imaging is extremely important. By using elastic SH RTM, we were able to clearly reproduce almost all reflectors inside the concrete model including the vertical step edges and the cross sections of the cavities. We were also capable to show that more features could be mapped compared to SAFT, and that imaging of complex reflectors could be sharpened compared to elastic P-SV (compressional-vertically polarized shear) RTM. Our promising results illustrate that elastic SH RTM has the potential to significantly enhance the reconstruction of challenging concrete structures, representing an important step forward for precise, high-quality ultrasonic NDT in civil engineering.

Keywords Concrete Structures · Ultrasonic Echo Technique · Elastic Reverse Time Migration · Synthetic Aperture Focusing Technique · Horizontally Polarized Shear Waves

1 Introduction

Quality assurance and structural investigation of concrete constructions are worldwide important tasks in civil engineering due to increasing traffic and aging infrastructure. To analyze the interior of new, repaired or rebuilt concrete structures without damaging them non-destructive testing (NDT) methods are used on a regular basis. A commonly used NDT method is the ultrasonic echo technique [1–3]. Typical applications include geometry determinations, thickness measurements and the detection of quality issues (honeycombing, cracks, and low concrete strength). Furthermore, the localization and characterization of built-in components, especially post-tensioned tendon ducts, is another important target [4, 5]. On the one hand, grouting defects in tendon ducts may reduce the durability of concrete structures [6, 7]. On the other hand, the precise localization and shape determination of tendon ducts is highly relevant since these built-in elements quite often are not installed exactly in accordance with the design plans. This can have a significant impact on the structure's load capacity [8].
The ultrasonic echo measurements are conducted from one side of a concrete object using transmitting and receiving transducers. Usually, lightweight dry-coupled point contact

✉ Maria Grohmann
maria.grohmann@bam.de

Ernst Niederleithinger
ernst.niederleithinger@bam.de

Stefan Maack
stefan.maack@bam.de

Stefan Buske
buske@geophysik.tu-freiberg.de

[1] Division Non-Destructive Testing Methods for Civil Engineering, BAM Federal Institute for Materials Research and Testing, Unter den Eichen 87, 12205 Berlin, Germany

[2] Institute of Geophysics and Geoinformatics, Technical University Bergakademie Freiberg, Gustav Zeuner Str. 12, 09599 Freiberg, Saxony, Germany

Published online: 24 November 2023

transducers are used, which can be coupled to the concrete surface by applying light pressure. These transducers are available for emitting and receiving shear (S) waves and compressional (P) waves in a frequency range of 25 - 200 kHz [9]. Currently, S-wave transducers, where the direction of particle oscillation is perpendicular to the plane of incidence (horizontally polarized shear, SH), are predominantly used. SH-waves do not convert to other types of waves at any contrast of impedance in two-dimensional (2D) media [10]. Hence, a less complex wavefield is generated and less scattering effects arise compared to P-wave excitation, where mode conversion to vertically polarized shear (SV) waves [11] and formation of surface waves in form of Rayleigh (R) waves will occur. For example, Mielentz et al. [12] demonstrated, that the signal-to-noise ratio of the measured ultrasonic data is better when using SH-wave transducer arrays than when using arrays of P-wave transducers. Moreover, SH-waves are totally reflected at free interfaces and at interfaces to liquids at all angles of incidence, which can be advantageous in ultrasonic examinations [13].

For data processing and imaging of measured data acquired with ultrasonic transducers synthetic aperture focusing technique (SAFT) algorithms [14] operating in time or frequency domain, or the closely related Total Focusing Method [15, 16] are generally used. In this study, we applied the time-domain SAFT algorithm, which is a diffraction stack, similar to the Kirchhoff prestack depth migration method [17] from geophysics. SAFT generates the ultrasonic image of the investigated concrete structure by numerically superimposing the reflected signals of single-sided measurements to the imaging points of the reconstructed area. More details on the SAFT algorithm can be found in [18, 19]. Improvements of the SAFT method using phase evaluation of the measured signal reflections to characterize reflectors has been published by Mayer et al. [20]. In numerous studies, the application of SAFT on concrete objects for, e.g., thickness measurements and the detection of defects, such as delaminations, cracks and grouting faults is presented [18, 21–29]. The localization of structural elements embedded in concrete objects by using SAFT, as for example tendon ducts, reinforcement and bore holes, has also been successfully investigated [5, 18, 21, 22, 24, 28, 29]. However, as a drawback, SAFT suffers from some limitations since only single reflections of the ultrasonic wavefield are considered for the imaging process. Multiple reflections and mode conversions of the wavefield originating from reflectors inside the concrete specimen are not taken into account and lead to the generation of imaging artefacts. Due to these limitations, the SAFT algorithm is not capable to image vertically or steeply dipping interfaces as well as complex structures such as steps and lower boundaries of voids. Furthermore, the ability to reconstruct hidden reflectors is limited. Hence, an accurate determination of the dimensions and geometries of complicated scattering bodies in concrete structures is not possible with SAFT. For example, the locations of tendon ducts can be assessed by using SAFT, but both the diameters and shapes of their cross sections can not be specified accurately.

For this reason, advanced migration techniques from geophysics such as one-way wave equation imaging were tested on ultrasonic data by Ballier et al. [30] in 2012. A further promising seismic migration technique called Reverse Time Migration (RTM) has the capability to produce even better imaging results of complicated structures in concrete. RTM is, in contrast to SAFT, a wave-equation based imaging technique and was originally introduced by Mc Mechan [31] and Baysal et al. [32] in 1983. A detailed overview on the theory of RTM is described in Sect. 2.1. Existing algorithms use the acoustic two-way (acoustic RTM) or the elastic two-way wave equation (elastic RTM) [33]. In the field of geophysics, acoustic RTM has been successfully applied, as for example to a complex salt dome model in hydrocarbon exploration [34] or to real seismic data for deep targeting and imaging of mineral deposits [35]. In recent years, acoustic RTM has also been tested on ultrasonic data in the field of NDT. In this study, our focus is on related work on the numerical and experimental application of RTM to ultrasonic data acquired on steel, concrete and reinforced concrete. For example, acoustic RTM was successfully applied to synthetic and real ultrasonic data for imaging defects within numerical steel models and inside a steel specimen [36, 37]. Müller et al. [38] effectively applied an acoustic RTM algorithm to synthetic acoustic ultrasonic echo data for geometry determination of 2D polyamide- and concrete-like models. The application of acoustic RTM to synthetic ultrasonic data for imaging defects within numerical concrete models and for localization of steel sleeves in numerical prefabricated concrete structures is presented in [39–41]. Moreover, in two preliminary studies, we successfully applied an acoustic RTM algorithm to synthetic ultrasonic data and real ultrasonic data acquired at a concrete foundation slab as well as a polyamide specimen [42, 43]. Compared to SAFT, the acoustic RTM results showed a significant improvement in imaging complex features inside both test specimens.

An RTM algorithm that uses the elastic wave equation instead of the acoustic one, has the potential to optimize the imaging results even further. This is due to the fact that our ultrasonic echo measurements on concrete are performed by exciting elastic waves. Generally, in exploration geophysics, elastic RTM algorithms that evaluate P-, SV- and R-waves (elastic P-SV RTM) are used to migrate seismic data generated by sources emitting P-waves [44–50]. Therefore, in a first elastic RTM study, we successfully evaluated the potential applicability of a 2D elastic P-SV RTM algorithm to image real ultrasonic echo data generated by P-wave transducers [51]. A 2D elastic P-SV RTM routine was tested on synthetic elastic ultrasonic data generated with a complex 2D concrete model.

By using our elastic P-SV RTM approach, we were able to improve significantly the imaging of complicated structures inside the model. Vertical reflectors and lower edges of complex built-in features, among others, could be reconstructed clearly which was not possible with the SAFT technique. Motivated by these promising results, our goal in this study was to investigate the potential of an 2D elastic RTM algorithm to image real ultrasonic data generated by SH-wave transducers (elastic SH RTM) since SH-waves are predominantly used for practical NDT applications. Therefore, we modified our 2D elastic P-SV RTM routine from [51] to a 2D elastic SH RTM routine capable of evaluating SH-wave data.

Numerous research studies have been published on the application of elastic RTM to ultrasonic data in NDT of steel, concrete and reinforced concrete structures. Anderson et al. [52] explored a fully experimental implementation of elastic RTM for the localization of a steel nut glued onto an aluminum plate. Furthermore, elastic RTM was successfully applied to synthetic and real ultrasonic data for detecting and imaging defects in steel models and steel specimens [53, 54] as well as in steel pipes [55]. Beniwal et al. [56] applied elastic RTM to focused synthetic and experimental ultrasonic data. It was shown by the authors, that the combination of elastic RTM with a focused ultrasonic P-wavefield is a promising technique for identifying defects around steel rebars in a concrete object. Nguyen et al. [57] developed a two-step workflow, combing full-waveform inversion and elastic RTM, for reconstruction of a delamination in two numerical concrete models. A further research paper for the application of elastic RTM on both synthetic and measured ultrasonic echo data was published by Liu et al. [58]. By using elastic RTM, the authors were able to evaluate the grouting compactness inside two splice sleeves of a precast concrete structure. Asadollahi et. al [59] developed an analytical elastic RTM approach to improve the efficiency of the RTM algorithm, reducing the memory demand and computation time needed. The authors validated their approach successfully using synthetic ultrasonic echo data from two different 2D concrete models. In a subsequent study, Asadollahi et al. introduced new imaging conditions to minimize high-amplitude artefacts and to obtain more precise amplitudes in elastic RTM images [60]. Büttner et al. [61] applied elastic RTM to synthetic and real ultrasonic echo data to investigate an engineered barrier for nuclear waste storage. The authors could enhance the imaging of deeper parts within the salt concrete test barrier, which contains inclined reflectors.

These studies present very clearly the advantages of elastic RTM for the imaging quality of synthetic and measured ultrasonic echo data acquired on steel, concrete and reinforced concrete. The main goal of almost all cited elastic RTM articles was the detection of flaws within the investigated structures. Asadollahi et al. [59], on the other hand, aimed to reconstruct exact geometries of structures inside two numerical concrete models. The objective of our study was also to determine the internal geometry of a 2D numerical concrete model, however it includes more complex structures. Moreover, the analytical approach presented by Asadollahi et al. [59] focusses on models with back wall structure parallel or inclined to the top edge whereas our elastic RTM routine is applicable to arbitrary geometries. In addition, we compare our elastic SH RTM images with the reconstruction results obtained by 2D elastic P-SV RTM and conventional 2D SAFT imaging. It must be further noted, that only in the studies of Asadollahi et al. [59, 60] and Büttner et al. [61] ultrasonic SH-waves were used for elastic RTM imaging, analogous to our elastic SH RTM study presented in this paper.

The investigated model in this paper corresponds to the concrete model used in our elastic P-SV RTM study [51]. It consists of a concrete layer surrounded by a layer of air and incorporating several steps and circular shaped cavities. The steps were included into the model since internal reflectors and external boundaries of concrete objects are often inclined or angled. The modeled circular cavities represent the usually circular cross section of tendon ducts. Using this model and our modified 2D elastic SH modeling routine numerous synthetic elastic SH data sets were generated. The application of elastic SH RTM and SAFT to the synthetic elastic SH data sets clearly demonstrates that by using elastic SH RTM more features inside the numerical concrete model could be detected and the imaging quality could be enhanced significantly. Moreover, compared to elastic P-SV RTM clearer and more precise images could be generated. Our research findings show that the usage of SH-wave transducers in combination with elastic SH RTM has the potential to allow for a more accurate determination of complex geometries in concrete objects than by using elastic P-SV RTM or SAFT imaging. Hence, elastic SH RTM is a step forward for imaging ultrasonic echo data in NDT.

This article is organized as follows: First we explain the RTM algorithm itself (Sect. 2.1). In Sect. 2.2, we present the 2D elastic SH finite difference modeling routine used. We further demonstrate our numerical concrete model (Sect. 2.3) and the generation of synthetic elastic SH-wave data (Sect. 3.1). Section 3.2 and Sect. 3.3 show the application of elastic SH RTM and SAFT reconstruction to the simulated elastic SH-wave data. Finally, in Sect. 4 we compare our elastic SH RTM results to the reconstruction results obtained using conventional SAFT imaging. Within this Section we further compare our elastic SH RTM images with the results from our elastic P-SV RTM study [51]. The paper ends with a conclusion and an outlook for future work (Sect. 5).

2 Materials and Methods

2.1 Principle of Reverse Time Migration

The RTM method, initially established for oil and gas exploration, is a depth migration algorithm that transforms the received signals as a function of recording time into features in the subsurface. RTM is, in contrast to the conventional applied SAFT technique, a wavefield-continuation method in time and uses the full wave equation. It is the only seismic migration method that is able to consider the entire wavefield including primary and multiple energy. Thus, multi-pathing and many other complex wave phenomena can be handled. RTM enables accurate mapping of steeply dipping reflectors and structures in areas with strong velocity variations. In addition, imaging artefacts caused by mistaking non-primary energy as primary energy can be reduced. The main disadvantage of the RTM technique is the extensive computing power and memory capacity required, especially for elastic RTM routines. Nonetheless, RTM has become attractive for the application in the field of NDT due to advances in parallel processing and other computational technologies.

Within the RTM algorithm, two independent wavefields are propagated through predefined models using usually a finite difference approximation of the acoustic or elastic wave equation [33]. By applying an imaging condition that combines both wavefields the final RTM image is generated. In this way, the received energy of the reflectors is focused back towards their location in the examined medium. The whole RTM imaging routine consists of five steps which are briefly described below. For further details, refer to our elastic P-SV RTM study [51], where the principle of the RTM imaging was additionally illustrated with two Figures. Steps two to four are performed individually for each source-receiver setup. The common source-receiver configuration in seismics, which was also used in this study, consists of a fixed shot point and multiple receiver positions along the line of measurement.

Step 1: Determination of a reasonable velocity and density model of the investigated medium including any a priori knowledge.

Step 2: The wavefield is propagated forward in time (starting at time zero) from the known source location using a source wavelet and the specific models from step 1. The result of this simulation is the so-called source wavefield W_S.

Step 3: The wavefield is propagated backward in time (starting at the maximum recording time) using the estimated models from step 1 and the recorded data (shot record) from measurements or simulations. Thereby, the receiver positions are converted into source locations and the shot record is reversed in time and injected at the source positions into the model domain. The result of this simulation is the so-called receiver wavefield W_R.

Step 4: This step includes the application of an imaging condition to W_S and W_R. In this study, we tested two imaging conditions (equation 1 and 2). The first imaging condition (equation 1) applied is the most common and robust imaging condition used in the seismic industry. To create the migrated section $I(x, z)$ it computes the zero-lag cross-correlation between the source and receiver wavefield W_S and W_R for every point in space (x,z) over the recording time T (cf. [62]):

$$I(x, z) = \sum_{t_i=0}^{T} W_S(x, z, t_i) \cdot W_R(x, z, t_i). \tag{1}$$

T denotes the maximum recording time and t_i is the time step. The main disadvantage of this imaging condition is the creation of low frequency, high amplitude noise in the area of sharp velocity contrasts, which can mask important structures inside the investigated models or real structures [63]. The cross-correlation imaging condition can be improved by a division through the intensity of the receiver wavefield [64]. This results in the receiver illumination imaging condition:

$$I(x, z) = \sum_{t_i=0}^{T} \frac{W_S(x, z, t_i) \cdot W_R(x, z, t_i)}{W_R^2(x, z, t_i)}. \tag{2}$$

Step 5: For the final result, the cross-correlation images $I(x, z)$ of all source-receiver configurations are summed up.

2.2 2D Elastic SH Finite Difference Modeling Algorithm

The 2D elastic SH finite difference modeling algorithm we used to perform the simulations of our synthetic ultrasonic data and to build our own elastic SH RTM routine is based on a 2D elastic P-SV finite difference algorithm included in the Madagascar open source software package [65]. The latter algorithm simulates the P-SV case in a 2D modeling domain and was used in our elastic P-SV RTM study presented in Grohmann et al. [51]. Table 1 shows the types of waves each elastic finite difference algorithm takes into account. Figure 1 illustrates the corresponding vibration and propagation directions of the wave types simulated in the x-z modeling

Table 1 Wave types modeled by 2D elastic finite difference algorithms

2D finite difference algorithm	Wave types
Elastic P-SV	Compressional - (P) vertically polarized shear (SV) and Rayleigh (R)
Modified elastic SH	Horizontally polarized shear (SH)

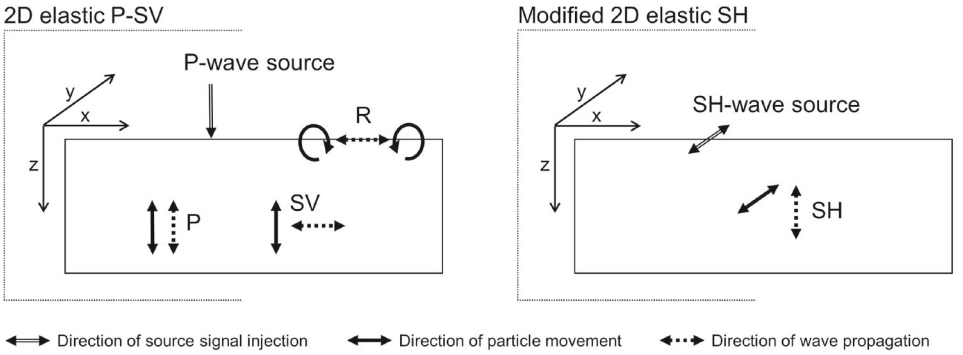

Fig. 1 Vibration and propagation directions of the simulated wave types in the x-z-modeling domain for the elastic P-SV and elastic SH finite difference modeling algorithm. For the P- and S-waves, only one of the possible wave propagation directions is sketched for simplification

plane. For the P- and S-waves, only one of the possible wave propagation directions is sketched for simplification. Using the elastic P-SV modeling routine and injecting a source signal into z-direction, P-waves, SV-waves and R-waves are formed. The particle vibration caused by P-waves is in the direction of wave propagation. For SV-waves, the particle displacement is perpendicular to the direction of wave propagation. In addition, high-amplitude R-waves are modeled whose particle motion is retrograde. Using the elastic SH simulation algorithm and injecting a source signal into y-direction produces the propagation of SH-waves in the x-z plane. Particle displacement takes place in y-direction perpendicular to the direction and plane of wave propagation. For this 2D case, SH-wave motion is completely decoupled from other wave types.

The 2D elastic SH finite difference code we applied in this study is parallelized using OpenMP and operates with a rotated staggered grid (RSG). It is second-order accurate in time and eighth-order accurate in space. Starting from the elastic P-SV finite difference code, we appropriately modified the differential equations (equations (2) to (5) in [51]) for the description of the propagation of SH-waves in the x-z plane. As explained above (Table 1 and Fig. 1) only shear stresses and strains connected to particle displacements in y-direction exist. Furthermore, we assumed a 2D medium with homogeneous isotropic materials. Elastic SH wave propagation in such a medium is calculated within our modified finite difference modeling routine by solving the following equations and neglecting external forces and boundary conditions:

1. Calculation of the components of the strain tensor ϵ:

$$\begin{aligned} 2\epsilon_{xy} &= \frac{\partial u_y}{\partial x}, \\ 2\epsilon_{yz} &= \frac{\partial u_y}{\partial z}, \end{aligned} \tag{3}$$

where (x,z) are the 2D spatial coordinates, ϵ_{xy} and ϵ_{yz} are the shearings. u_y denotes the particle displacement vector wavefield.

2. Calculation of the components of the stress tensor σ:

$$\begin{aligned} \sigma_{xy} &= 2C_{66}\epsilon_{xy}, \\ \sigma_{yz} &= 2C_{44}\epsilon_{yz}, \\ with: C_{66}, C_{44} &= \mu, \end{aligned} \tag{4}$$

where σ_{xy} and σ_{yz} denote the two shear stresses. C_{44} and C_{66} are elements of the stiffness tensor with μ beeing the Lamé constant.

3. Calculation of particle acceleration vector wavefield a_y:

$$a_y = \frac{1}{\rho}\left(\frac{\sigma_{xy}}{\partial x} + \frac{\sigma_{yz}}{\partial z}\right), \tag{5}$$

where ρ denotes the density.

4. Performing the time update by the calculation of particle-displacement vector wavefield u_y at time $k+1$:

$$u^{k+1}_{y_{i,j}} = a_{y_{i,j}} dt^2 - u^{k-1}_{y_{i,j}} + 2u^{k}_{y_{i,j}}, \tag{6}$$

where t is the travel time. i, j and k are the indexes for the x-axis discretization, the z-axis discretization and for the time-axis discretization. dt is the grid step in time. Grid spacing is equal in x- and z-direction.

Discretization and approximation of the temporal and spatial derivatives within the elastic SH finite difference algorithm is analogous to the elastic P-SV algorithm presented in [51]. Corresponding details can be found there.

2.3 Numerical Model and Boundary Conditions

For the generation of the synthetic elastic SH ultrasonic data, we defined the same 2D numerical concrete model we used in [51]. It corresponds in its geometry to one of our concrete reference specimens at BAM. Details on this specimen are summarized in [66]. The used 2D model contains a three-step homogeneous concrete layer surrounded by a 0.02 m

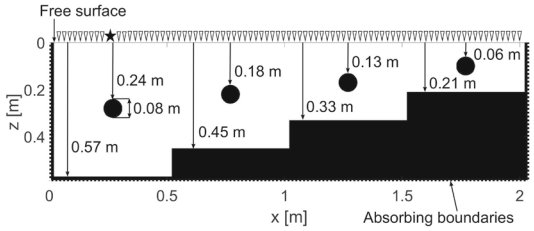

Fig. 2 2D numerical three-step concrete model with absorbing boundaries at the sides and lower edge (marked with a dashed line) and a free surface at the top edge (adapted from [51]). As an example, the position of shot point No. 11 is marked with a black star and the receiver positions are indicated with triangles

Table 2 Material parameters used for concrete and air layer

	Concrete	Air
Shear wave velocity $\mathbf{v_S}$ $[\frac{m}{s}]$	2750	0
Density$[\frac{kg}{m^3}]$	150	1.2

thick layer of air at the side edges and at the lower edge. The whole model is 2.04 m wide and 0.59 m deep. The concrete layer incorporates four circular cavities with a diameter of 0.08 m at the mid-depth of the corresponding sub-sections. The depths of the cavities and the different thicknesses of the concrete layer are shown in Fig. 2. The material parameters used for modeling are summarized in Table 2. A density value of 150 kg/m^3 for concrete was used instead of the correct value of 2400 kg/m^3 since using the true density value caused instability problems of the elastic simulations. Analogous to the elastic P-SV finite difference algorithm used in [51], the elastic SH finite difference algorithm does not perform arithmetic averaging of the density, which is important for stable simulation results at interfaces with large impedance contrasts [67]. In our elastic P-SV RTM study [51], we were able to demonstrate that using a density value of 150 kg/m^3 instead of 2400 kg/m^3 for concrete does not have a large effect on the amplitudes of the RTM result and is therefore a valid approximation.

Analogous to our elastic P-SV RTM study [51] we defined absorbing boundaries at the lateral and lower boundaries of our model domain (marked with a dashed line in Fig. 2). The absorbing boundary condition is realized within the elastic SH modeling algorithm by the combination of the Clayton and Enquist [68] boundary and the boundary of Cerjan [69]. It must be mentioned that the absorbing boundary condition applied here was adapted from our elastic P-SV RTM study and does not work perfectly for the 2D SH case. The SH wavefield is not completely absorbed at the model boundaries. The same observation is described in [70]. However, since the SH waves are totally reflected at the concrete-air interfaces the absorbing boundary condition is not essential for the 2D concrete model used in this study and can be neglected. Furthermore, a free surface was assumed for the top edge of the model space where the sources and receivers are positioned (labelled in Fig. 2) to ensure a total reflection of the wavefield energy. Therefore, the two shear stresses σ_{xy} and σ_{yz} above the free surface boundary were set to zero.

3 Results

3.1 Simulation of Elastic SH Synthetic Ultrasonic Echo Data

In a first step, elastic synthetic SH data were generated for imaging with RTM, using the elastic finite difference algorithm presented in Sect. 2.2. The parameters used for simulation are listed in Tables 3 and 4. Due to the spatial sampling interval of 0.0005 m, the model size is 4080 grid points in x- and 1180 grid points in z-direction. The temporal sampling interval was set to $1 \cdot 10^{-8}$ s. The simulation time of 0.00087 s was chosen to include different wave paths as for example the elastic SH wavefield which is directly reflected at the lower boundary of the first chavity and propagating from there to the lower boundary of the concrete layer and then back to the receivers. Since our ultrasonic echo measurements are usually conducted from one side of a concrete specimen, we defined 99 point sources, each with 199 point receivers, on the surface of our 2D model (marked exemplarily for source position No. 11 in Fig. 2). As source signal for simulation of elastic synthetic SH data and for modeling the source wavefield W_S (see Sect. 2.1 step 2) a Ricker wavelet [71, 72] was used with a time delay of t_0 = 0.04 ms and a center frequency of 50 KHz, since the SH-wave transducers we use for real ultrasonic echo measurements are excited at this frequency. Using the concrete shear wave velocity (Table 2), the temporal and spatial sampling interval and the coefficients of the eighth-order RSG finite difference scheme introduced in [51], the von Neumann stability criterion for an RSG presented by Saenger et al. [73] is fully satisfied.
The elastic SH wavefield simulations were performed on a High Performance Computing (HPC) Linux (CentOS 7)-Cluster at BAM. The HPC Cluster comprises in total 25 nodes

Table 3 Simulation parameters

Simulation parameter	
Model size [grid points]	4080 (x) x 1180 (z)
Spatial sampling interval [m]	0.0005
Simulation time [s]	0.00087
Temporal sampling interval [s]	$1 \cdot 10^{-8}$
Frequency Ricker wavelet [kHz]	50
Wavelet delay [s]	0.00004

Table 4 Coordinates of sources and receivers

	Sources	Receivers
Number	99	199
Distance [m]	0.02	0.01
Position of source and receiver No. 1 [m]	$x = 0.04$	$x = 0.03$

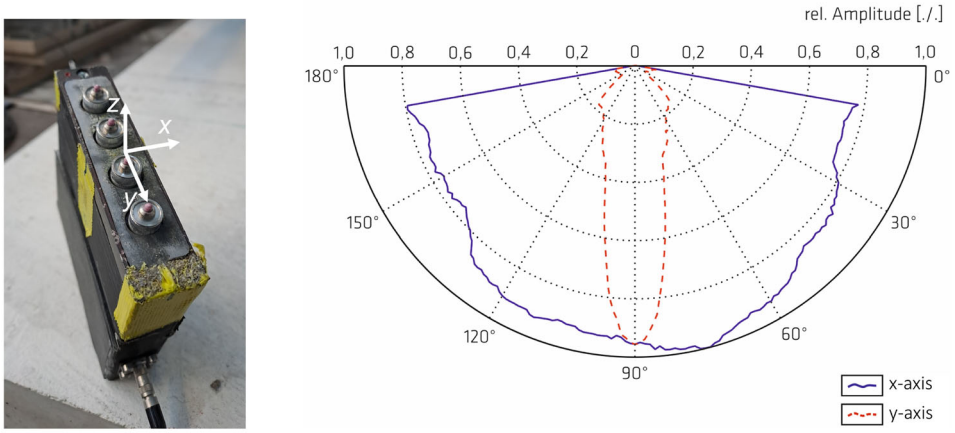

(a) (b)

Fig. 3 **a** S-wave transducer array and **b** directivity pattern of the transducer shown in (**a**) for exciting SH-waves

with 1720 CPU Cores, 8 TB RAM and 77 TB hard disk space. The simulations were generally performed on four nodes of the HPC Cluster, each having the following characteristics: 4 (Intel Xeon E7-8880 v4) CPUs with 22 cores and 2,2 GHz clock speed as well as 11,6 GB RAM per core. For example, the computational time required for the simulation of the elastic SH data for one source position was 45 min on a node.

At the receiver locations the acceleration components of the elastic SH wavefields were read out. At the source positions, we injected the Ricker wavelet as acceleration signal into y-direction since the radiation pattern of an acceleration source (Fig. 5a) corresponds rather to the directivity pattern of the ultrasonic S-wave transducers we apply. Figure 3a shows one of our two ultrasonic S-wave transducer arrays we use for collecting the measurement data. Here the x-, y- and z-direction correspond to the x-, y- and z-axis in our numerical model. In one casing four point contact S-wave transducers are arranged in a row and connected in parallel. Since we use SH-waves the polarization of the excited shear waves is in y-direction perpendicular to the measurement direction (x-direction). This arrangement of point contact transducers generates an ultrasonic wavefield which is focused like a disc below the measurement profile. To investigate the exact shape of the generated ultrasonic wavefield, measurements were conducted with the ultrasonic S-wave transducer array on a semi-sphere of self-compacting concrete. Theoretical details as well as information concerning the measurement setup and the half-sphere concrete specimen were published in [74]. Figure 3b shows the determined directivity pattern in a polar diagram. The distribution of the maximum amplitude

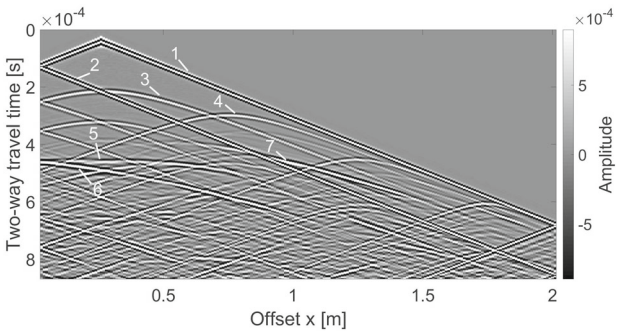

Fig. 4 Elastic SH data of shot point No. 11: y-component of acceleration. No. 1, 2, 3, 4, 5, 6 and 7 mark essential wave events

per directional angle is shown (the amplitudes were normalized to 1). The blue curve represents the distribution of the maximum amplitude in x-direction (direction of the measurement profile) and the red curve illustrates the distribution in y-direction perpendicular to the measurement direction. We can observe that the maximum amplitude is almost evenly distributed on a semicircle and does not drop below 75 %. Due to the limited mechanical range of the used measurement setup, the directivity pattern can only be determined between 10° and 170°. Furthermore, by arranging the four point contact transducers in one row a focusing of the ultrasonic wavefield in x-direction is achieved. Hence, the elastic SH data can be evaluated two-dimensionally.

Figure 4 and Fig. 5 exemplarily show the generated elastic synthetic SH data and elastic SH wavefield snapshots at times $t = 0.0001$ s, $t = 0.0002$ s, $t = 0.00029$ s and $t = 0.000463$ s for source position No. 11 located at $x = 0.26$ m above the first

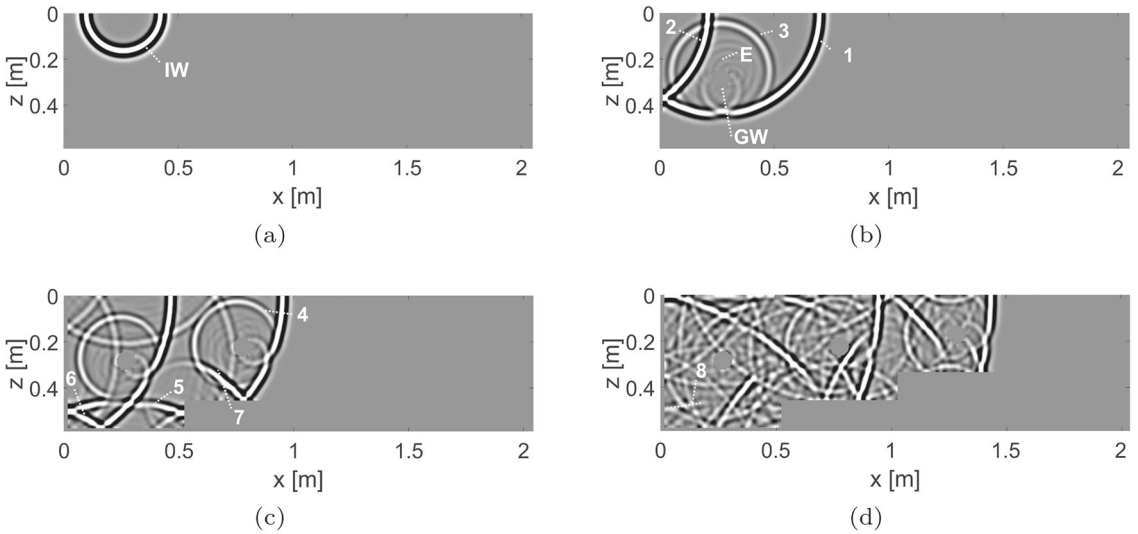

Fig. 5 Snapshots of elastic SH acceleration wavefield of shot point No. 11 at times: **a** t = 0.0001 s, **b** t = 0.0002 s, **c** t = 0.00029 s and **d** t = 0.000463 s. No. 1, 2, 3, 4, 5, 6, 7, 8 and the letters IW, E and GW mark essential wave events

cavity. The amplitudes of the y-component of acceleration are shown and essential wave events are highlighted accordingly. The elastic SH wavefield snapshot at time t=0.0001 s shows the incident elastic SH wavefield (IW). Furthermore, the direct wave (1) and the reflection of the direct wave at the upper left edge of the concrete layer (2) are visible. Reflection hyperbolas caused by the first (3) and second cavity (4) can be seen. Furthermore the reflection of the SH wavefield at the lower boundary of the concrete layer (5) and at the lower left edge of the concrete layer (6) are visible. Further on, the reflection event of the incident SH wave at the corner of the first step can be clearly seen (7). The snapshot of the elastic SH wavefield at time t = 0.000463 s highlights the reflection of the SH wave at the lower boundary of the concrete layer (8), which was previously reflected at the lower edge of the first cavity. This wave event is not clearly visible in the y-component of the elastic SH data. Moreover, in the elastic wavefield snapshot at time t = 0.0002 s, a guided wave (GW) is observable propagating along the boundary of the cavity and radiating energy (E) back into the concrete layer.

3.2 Elastic SH Reverse Time Migration of Synthetic Ultrasonic Echo SH Data

For elastic SH RTM evaluation of the 99 simulated elastic SH shot records the simulation and material parameters from Tables 2, 3 and 4 were used. Furthermore, the RTM analysis was performed iteratively (Fig. 6). After each RTM evaluation, an updated migration model was generated that contained new information and resulted in an improved RTM image. As features to be included into the updated migration models we specified elements of the reconstructed outer boundary of the numerical concrete model since these represent the deepest reflectors where the elastic wavefield is reflected back into the concrete medium. For numerical and real concrete structures, it is always reasonable to first localize the outer boundaries and include them into updated migration models in order to realize and improve the imaging of internal geometries. The source and receiver wavefields W_S and W_R can only cross-correlate correctly in time inside the concrete layer if the outer edges are known.

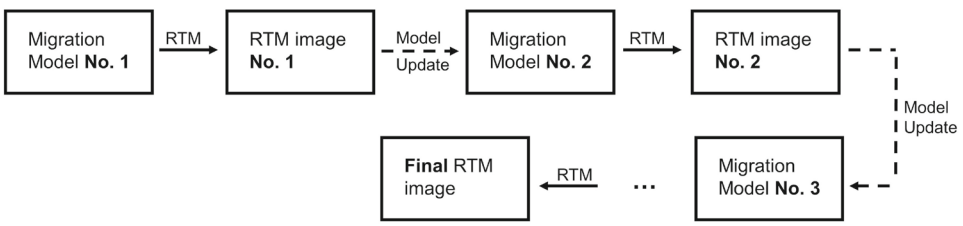

Fig. 6 Iterative RTM evaluation method

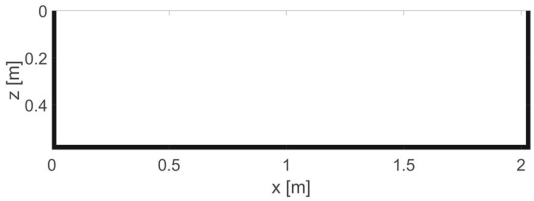

Fig. 7 Structure of the velocity and density model used for the first elastic SH RTM (taken from [51])

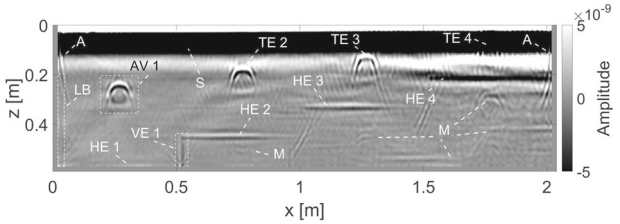

Fig. 8 Elastic SH RTM result obtained using the migration model presented in Fig. 7 (AV 1: first cavity, TE 2, TE 3 and TE 4: top edges of the second, third and fourth cavity, VE 1: vertical edge of the first step, HE 1, HE 2, HE 3 and HE 4: lower boundary of the concrete layer at different depths, LB: left lateral boundary of the concrete layer, A and M: migration artefacts)

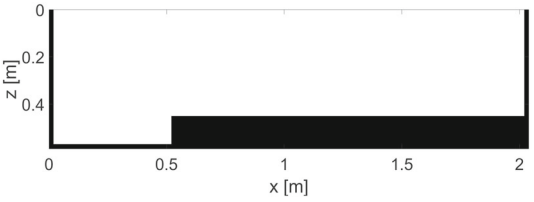

Fig. 9 Structure of the velocity and density model used for the second elastic SH RTM (taken from [51])

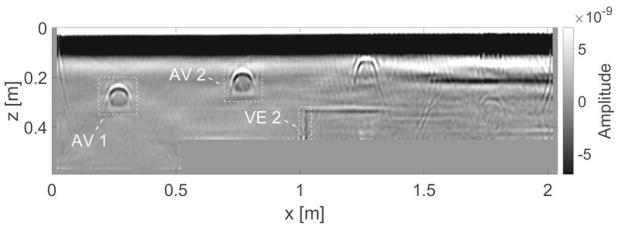

Fig. 10 Elastic SH RTM result obtained using the migration model presented in Fig. 9 (VE 2: vertical edge of the second step, AV 1: first cavity and AV 2: second cavity)

For different concrete models than presented in this study it may additionally be useful to incorporate successfully reconstructed reflectors that are part of the internal geometry into updated migration models. However, this was not necessary for our numerical model. For our RTM study, a total of four RTM calculations were required for a satisfactory result. The computational time required for an entire elastic SH RTM analysis distributed over four nodes of the HPC Cluster available at BAM was 46 h and 29 min.

For the first elastic SH RTM evaluation, we assumed the horizontal and maximum vertical extension of the concrete layer to be known (Fig. 7). The corresponding elastic SH RTM result after zero-lag cross-correlation between the acceleration source wavefield W_S and the acceleration receiver wavefield W_R is shown in Fig. 8. It demonstrates the successful reconstruction of the lower edge of the concrete layer (HE 1, HE 2, HE 3 and HE 4). The vertical edge of the first step was also imaged clearly at the correct position at $x = 0.52$ m (dashed rectangle VE 1). Further on, the complete cross section of the first cavity including the lower edge was successfully reproduced (dashed square AV 1). The top edges of the second and third cavity (TE 2 and TE 3) were imaged successfully whereas the top edge of the fourth cavity (TE 4) is obscured by a strong near-surface artefact (S). This artefact arises from unwanted cross-correlations of high amplitude direct waves. Moreover, the left lateral boundary of the concrete layer is visible in the RTM image (dashed rectangle LB) from a depth of about $z = 0.2$ m. The upper part of this boundary and the entire right lateral boundary are hidden by arc-like migration artefacts (A). These artefacts result from cross-correlations between incident waves of the source wavefields W_S and wavefronts of the receiver wavefields W_R which are generated by the direct waves reflected at the upper edges of the concrete layer (see for example event No. 2 in Fig. 4). Additional migration artefacts caused by unwanted cross-correlations can be observed. For example, the events marked with the letter M are generated by multiple reflections at the cavities and at the lower boundary of the concrete layer. Since we were able to successfully reconstruct the first concrete step, it was integrated into a second migration model (Fig. 9). The second elastic SH RTM result (Fig. 10) illustrates the successful imaging of the vertical edge of the second step (dashed rectangle VE 2) and the reconstruction of the complete cross section of the second cavity (dashed square AV 2). In addition, imaging of the first cavity could be improved (dashed square AV 1). For a next elastic SH RTM evaluation, the two steps already reconstructed were integrated into a third migration model (Fig. 11). The corresponding elastic SH RTM image after zero-lag cross-correlation of W_S and W_R can be seen in Fig. 12. The vertical edge of the third step (dashed rectangle VE 3) and the complete shape of the third cavity (dashed square AV 3) were imaged clearly. Moreover, imaging of the second cavity could be enhanced (dashed square AV 2). For a final elastic SH RTM calculation, all three reconstructed steps were put into a fourth migration model (Fig. 13). Using this three-step model, imaging of the fourth cavity was achieved (dashed square AV 4 in Fig. 14) despite the strong near-surface artefact. Further on, reconstruction of the third cavity could be improved (dashed square AV 3 in Fig. 14).

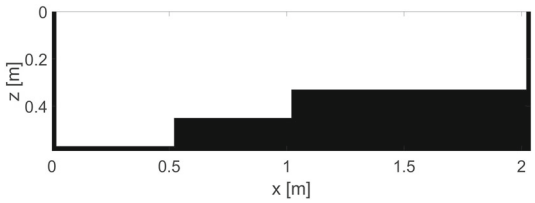

Fig. 11 Structure of the velocity and density model used for the third elastic SH RTM (taken from [51])

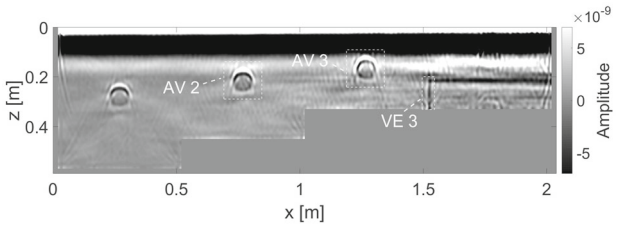

Fig. 12 Elastic SH RTM result obtained using the migration model presented in Fig. 11 (VE 3: vertical edge of the third step, AV 2: second cavity and AV 3: third cavity)

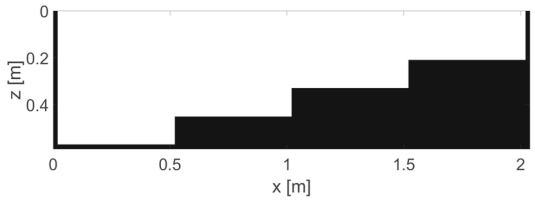

Fig. 13 Structure of the velocity and density model used for the fourth elastic SH RTM (taken from [51])

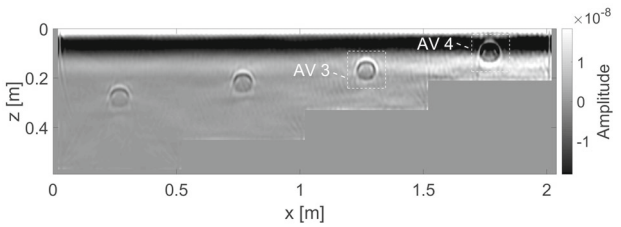

Fig. 14 Elastic SH RTM result obtained using the migration model presented in Fig. 13 (AV 3: third cavity and AV 4: fourth cavity)

By applying the presented multi-stage RTM evaluation to our 99 synthetic elastic SH shot records, we were able to successfully image all reflectors in the model, except for the right lateral edge of the concrete layer. Moreover, it is noticeable that in the presented RTM images the amplitudes of the lower edges of the circular cavities No. 1, No. 2 and No. 3 are weaker than the amplitudes of other reflectors. This is due to the fact, that direct reflections at the lower edges of the first three cavities are not visible in the receiver data. Therefore, the wavefields diffracted at these edges are used for their reconstructions. To raise the amplitudes of the lower edges of these cavities, we applied the receiver illumination imaging condition (see equation 2 in Sect. 2.1) to the RTM wavefields generated for the final RTM result (Fig. 14). Figure 15 shows the corresponding RTM image. Compared to Fig. 14 the lower edges of the first three cavities (LE 1, LE 2 and LE 3 in Fig. 15) are reconstructed with higher amplitudes. Furthermore, to suppress the strong near-surface artefact (letter S in Fig. 8) which represents low wavenumbers, we exemplarily processed the final RTM image (Fig. 14) with a Laplacian edge detection filter [75]. Figure 16 shows the corresponding RTM result. The strong near-surface artefact could be removed successfully, resulting in a significantly improved imaging of the fourth cavity (AV 4 in Fig. 16).

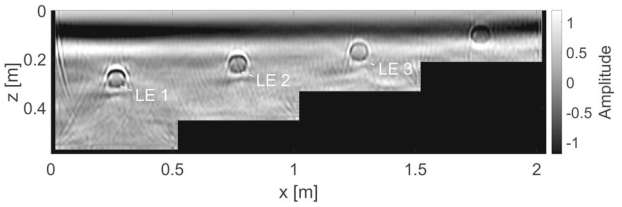

Fig. 15 Elastic SH RTM result obtained using the migration model presented in Fig. 13 and after applying the receiver illumination imaging condition (lower edges of the LE 1: first cavity, LE 2: second cavity and LE 3: third cavity)

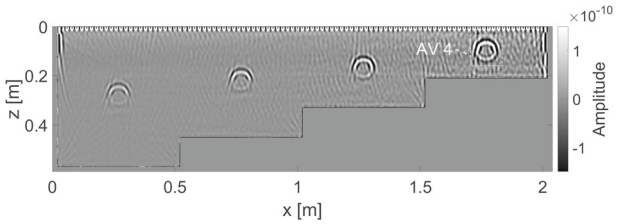

Fig. 16 Elastic SH RTM result obtained after applying a Laplacian edge detection filter to the RTM imaging result shown in Fig. 14 (AV 4: fourth cavity)

3.3 SAFT-Imaging of Synthetic Ultrasonic Echo SH Data

Figure 17 shows the imaging result obtained by the homogeneous 2D SAFT analysis of the 99 elastic SH shot records. We used the Intersaft software [76] to calculate the SAFT reconstructions and a homogeneous velocity model with $v = 2750\,\text{m/s}$. To allow a better comparison with the RTM results we obtained it would be more appropriate to perform further SAFT reconstructions with velocity models containing a priori information. Unfortunately, this is not possible at the moment with the SAFT software available to us.

In the obtained SAFT-reconstruction (Fig. 17), the lower boundary of the concrete layer at $z = 0.57$ m and the edges of the steps running parallel to the top edge of the model are clearly visible (HE in Fig. 17). Furthermore the top edges of the four cavities were imaged successfully (TE in Fig. 17). Migration artefacts due to multiple reflections in the syn-

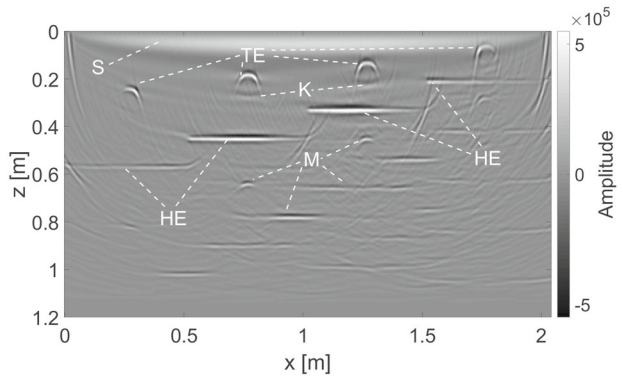

Fig. 17 2D SAFT result of 99 elastic SH shot records (TE: upper edges of the four cavities, HE: step edges running parallel to the surface of the model, K: migration artefacts due to creeping waves, M: migration artefacts due to multiple reflections in the synthetic data and S: near-surface artefact)

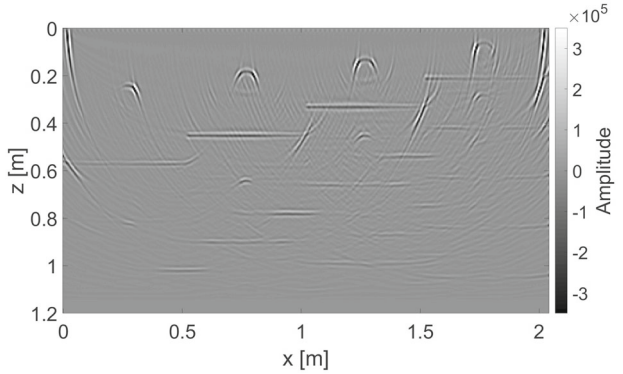

Fig. 18 2D SAFT obtained after applying a Laplacian edge detection filter to the SAFT imaging result shown in Fig. 17

thetic data can be clearly seen (marked exemplarily with M in Fig. 17). The imaging artefacts marked with the letter K in Fig. 17 are caused by the creeping waves which rotate around the cavities and thus enter their shadow area [29]. Moreover, analogous to the elastic SH RTM results a near-surface artefact (S in Fig. 17) is visible due to the high-amplitude direct waves in the synthetic data. This artefact can be removed with applying a Laplacian edge detection filter (Fig. 18).

4 Comparison of Elastic SH RTM with Elastic P-SV RTM and SAFT-Imaging

Figure 19 and Table 5 show a summary comparison of reconstructed features of the numerical three-step concrete model (Fig. 2) using the two imaging techniques applied in this paper: elastic SH RTM and SAFT. For this purpose, selected image details from the results shown in Sect. 3.2 and 3.3, which show specific structural elements of the numerical concrete model, are presented in Table 5. To evaluate the

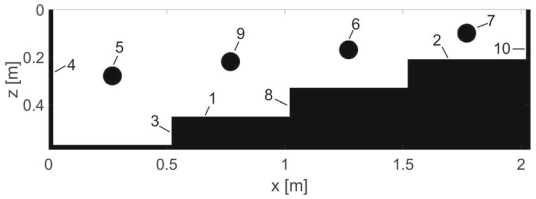

Fig. 19 2D numerical concrete model (structural features are labeled with numbers, which correspond to the numbers in the first column of Table 5 and Table 6 (adapted from [51])

potential of our elastic SH RTM results compared to the findings presented in our preliminary elastic P-SV RTM article [51] a separate Table (Table 6) was created. The numbers in the first column of Table 5 and Table 6 correspond to the numbers in Fig. 19.

Comparing elastic SH RTM and SAFT we can see that the boundary of the concrete layer at $z = 0.57$ m and the further edges of the steps running parallel to the surface of the concrete layer were reproduced with both imaging algorithms but with different reconstruction quality. For example, the horizontal edge of the first step was imaged with weak amplitude at the foot of the second step by using elastic SH RTM (No. 1: marked with a dashed white rectangle). In the SAFT result this part of the horizontal edge was reproduced with higher amplitude (No. 1: marked with a dashed white rectangle). However, the third horizontal step edge located in the thinnest area of the concrete layer where the most complex elastic wavefield is formed, was imaged with higher amplitude near the right lateral boundary of the concrete layer using elastic SH RTM compared to SAFT (No. 2: marked with dashed rectangles). Further on, the vertical edges of the three steps (No. 3: marked exemplarily with dashed rectangles for the first step) were reconstructed successfully with elastic SH RTM. It is evident, that imaging of these edges was not achieved with SAFT reconstruction. Moreover, the left lateral edge of the concrete layer (No. 4: marked with dashed rectangles) could be reproduced with elastic SH RTM, whereby the upper part of this edge is hidden by an artefact. Analogous to the vertical step edges, reconstruction of this vertical feature was not possible with SAFT imaging. The right lateral boundary of the concrete layer could not be reproduced by either imaging algorithm (No. 10 in Fig. 19). The observation of the four cavities (No. 5, No. 6 and No. 7: shown exemplarily for the first, third and fourth cavity) illustrates that elastic SH RTM was able to map their cross sections completely and accurately. SAFT was able to image a large part of the upper boundaries of the four cavities, however, reconstruction of the lower edges of these reflectors could not be achieved (No. 5, No. 6 and No. 7: marked exemplarily with dashed rectangles). Due to the capability of elastic SH RTM to image the entire cross sections of all four cavities their diameter of 8 cm can be determined accurately (marked

Table 5 Comparison of elastic SH RTM with SAFT Imaging

Structural Element	Elastic SH RTM (E)	SAFT Imaging (S)
1. Horizontal edge of first step (taken from: Fig. 8 (E) and Fig. 17 (S))		
2. Horizontal edge of third step (taken from: Fig. 8 (E) and Fig. 17 (S))		
3. Vertical edge of first step (taken from: Fig. 8 (E) and Fig. 17 (S))		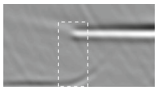
4. Left lateral edge concrete layer (taken from: Fig. 8 (E) and Fig. 17 (S))		
5. Cross section of first cavity (taken from: Fig. 8 (E) and Fig. 17 (S))	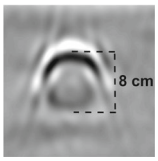	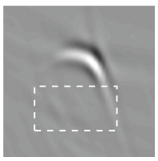
6. Cross section of third cavity (taken from: Fig. 14 (E) and Fig. 17 (S))	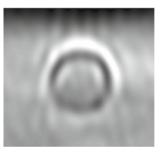	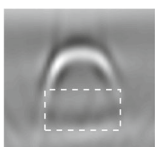
7. Cross section of fourth cavity (taken from: Fig. 16 (E) and Fig. 18 (S))	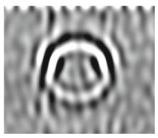	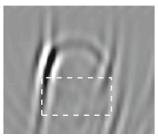

exemplarily for the first cavity No. 5). By using SAFT, the diameters of the cavities can merely be estimated.

For the comparison of elastic SH RTM with elastic P-SV RTM [51], three selected features are depicted in Table 6: the horizontal edge of the third step, the vertical edge of the second step and the cross section of the second cavity. For elastic P-SV RTM the cross-correlation results of the z- and x-components of the acceleration wavefields are shown. It is evident, that for the three structural elements presented, an enhanced imaging result was obtained by applying elastic SH RTM. The reflectors inside the numerical concrete model were imaged more clearly and continuously and with fewer migration artefacts compared to elastic P-SV RTM. Here it must be mentioned, that the elastic P-SV RTM results of the z- and x-component complement each other due to the directivity characteristics of P- and SV-waves [51]. For example, the imaging result of the z-component of the second cavity (No. 9) shows a better mapping of the top and lower edge whereas the imaging result of the x-component illustrates a better reconstruction of the lateral edges (marked with arrows: No. 9). The further reflectors of the numerical concrete model, which were imaged with elastic P-SV RTM and are not shown in Table 6, were also reproduced more precisely by using elastic SH RTM, especially the vertical step edges and the cross sections of the cavities. For more details refer to Grohmann et al. [51].

The above comparison of elastic SH RTM with elastic P-SV RTM and SAFT clearly demonstrates the advantages of elastic SH RTM. The reflectors inside the numerical concrete model could be reconstructed most exactly and accurately with elastic SH RTM. Firstly, the comparison of elastic SH RTM with elastic P-SV RTM shows the disadvantages of elastic P-SV RTM. A more complex elastic wavefield is processed by using elastic P-SV RTM since three different wave types (P-, SV- and R-waves) and mode conversions are taken into account. In addition, high amplitude R-waves lead to stronger edge reflections. As a result, more migration artefacts are formed and the imaging quality is not as high as by

Table 6 Comparison of elastic SH RTM with elastic P-SV RTM

Structural Element	Elastic SH (SH)	Elastic P-SV z-component (Z)	**Elastic P-SV** x-component (X)
2. Horizontal edge of third step (taken from: Fig. 10 (SH), [51] (Z) and [51] (X))			
8. Vertical edge of second step (taken from: Fig. 10 (SH), [51] (Z) and [51] (X))	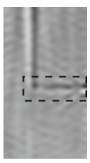	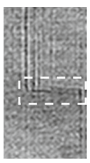	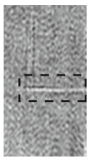
9. Cross section of second cavity (taken from: Fig. 14 (SH), [51] (Z) and [51] (X))	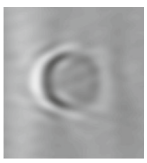	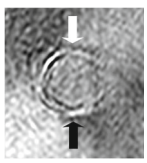	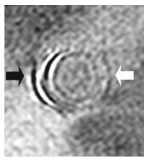

using elastic SH RTM. Furthermore, the comparison between the elastic SH RTM and SAFT results illustrates the disadvantages of the SAFT algorithm, analogous to the findings presented in our acoustic RTM articles [42, 43] and our elastic P-SV RTM study [51]. The SAFT algorithm is based on the approximate integral solution of the wave equation and normally considers only the shortest wave paths between sources and receivers. Hence, for a concrete structure with strong velocity contrasts and the associated changes of the wave propagation paths, no adequate migration result can be achieved [77]. As a result, none of the vertical reflectors could be imaged, nor any of the lower edges of the cavities. RTM, in contrast, directly solves the wave equation and is thus more precise. Due to the usage of the full wave equation all wave effects are taken into account, allowing the imaging of reflectors with inclinations $> 70°$, even in media with strong velocity variations. Despite the mentioned limitations of SAFT, a combination between RTM and SAFT can be very useful. Depending on the use case, the SAFT algorithm could be used for an initial analysis to correctly determine the location of the lower edge of a concrete object. This would require fewer RTM evaluations to be performed as these are significantly more time and computationally intensive than SAFT analyses [51].

5 Conclusions and Future Work

In this paper, the applicability of a 2D elastic SH RTM algorithm to image ultrasonic echo data generated by SH-wave transducers was evaluated based on synthetic data. For this purpose, 99 elastic shot records were simulated with a complex numerical concrete model containing three steps and four circular cavities. Our imaging results show that, in contrast to SAFT, elastic SH RTM was capable to detect more features inside the numerical model whereby the imaging quality of the structural elements could be enhanced significantly. Moreover, the reconstruction quality of the searched reflectors inside the concrete model is considerably higher in the elastic SH RTM images compared to the elastic P-SV RTM results presented in our first elastic RTM study [51]. Hence, elastic SH RTM is a step forward for ultrasonic NDT of challenging concrete structures.

Specifically, the complete cross sections of the four cavities could be imaged clearly allowing the accurate determination of their diameters. This would not have been possible with traditional SAFT imaging. Moreover, in contrast to SAFT, vertical borders could be imaged, in particular the left lateral boundary of the concrete layer and the vertical step edges. Reconstruction of the lower boundary of the concrete layer in the thinnest part of the model (at $z = 0.21$ m) where the most complex elastic wavefield is formed, could also be improved with elastic SH RTM. Compared to elastic P-

SV RTM clearer images of the reflectors inside the concrete model were produced with less migration artefacts. Especially, reconstruction of the cross sections of the cavities and vertical step edges could be sharpened.

Motivated by our promising results, there are several aspects we would like to address in future work. First, we will test the applicability of our 2D elastic SH RTM algorithm to image measured ultrasonic echo data generated with SH-wave transducers. Corresponding ultrasonic echo measurements have already been performed at one of our laboratory concrete specimens, whose geometry is similar to the numerical model presented in this paper. Second, the absorbing boundary condition needs to be improved in order for the elastic SH RTM algorithm to provide more accurate imaging results for NDT applications where the concrete structure is not surrounded by a liquid and/or gas. Furthermore, the elastic RTM algorithm should be extended to three dimensions.

Acknowledgements Many thanks to our colleagues at BAM 8.2, especially Vera Lay. Big thanks also goes to our colleagues in the IT department for the support of the computationally intensive elastic Reverse Time Migration calculations. Klaus Mayer of the University of Kassel (Germany) adapted the SAFT algorithm for the imaging of our synthetic ultrasonic SH-wave data. Thanks to him for providing the modified algorithm. We also thank Olaf Hellwig and Christoph Büttner from the Technical University Bergakademie Freiberg for their fruitful discussions concerning the implementation of the elastic SH RTM algorithm.

Author Contributions MG: Conceptualization, Methodology, Investigation, Software, Formal Analysis, Writing - Original Draft, Data Interpretation & Analysis. EN: Supervision, Conceptualization, Writing - Review & Editing. SM: Formal Analysis, Writing - Review & Editing. SB: Writing - Review & Editing.

Funding Open Access funding enabled and organized by Projekt DEAL. No funding was received for conducting this study.

Availability of Data and Material Data and material are available from the corresponding author upon request.

Declarations

Conflict of Interest Not applicable.

Ethical Approval and Consent to Participate Not applicable.

Consent for Publication Not applicable.

References

1. Schickert, M., Krause, M.: Ultrasonic techniques for evaluation of reinforced concrete structures. In: Maierhofer, C., Reinhardt, H.-W., Dobmann, G. (eds.) Non-destructive Evaluation of Reinforced Concrete Structures, vol. 2, pp. 490–530. Woodhead Publishing Limited, Sawston, Great Britain (2010). https://doi.org/10.1533/9781845699604.2.490
2. Krause, M.: Localization of grouting faults in post tensioned concrete structure. In: Breysse, D. (ed.) Non-Destructive Assessment of Concrete Structures: Reliability and Limits of Single and Combined Techniques, pp. 263–304. Springer, Berlin, Germany (2012). https://doi.org/10.1007/978-94-007-2736-6_6
3. Niederleithinger, E., Wolf, J., Mielentz, F., Wiggenhauser, H., Pirskawetz, S.: Embedded ultrasonic transducers for active and passive concrete monitoring. Sensors **15**(5), 9756–9772 (2015). https://doi.org/10.3390/s150509756
4. Krause, M., Milmann, B., Schickert, M., K., M.: Investigation of tendon ducts by means of ultrasonic echo methods: A comparative study. Paper presented at the European conference on NDT, Berlin (2006)
5. Krause, M., Mayer, K., Friese, M., Milmann, B., Mielentz, F., Ballier, G.: Progress in ultrasonic tendon duct imaging. Eur. J. Environ. Civ. Eng. (2011). https://doi.org/10.1080/19648189.2011.9693341
6. Eichinger, E.M., Diem, J., J., K.: Bewertung des Zustandes von Spanngliedern auf der Grundlage von Untersuchungen an Massivbrücken der Stadt Wien. Institut für Stahlbeton und Massivbau (1) (2000)
7. Vogel, T.: Zustandserfassung von Brücken bei deren Abbruch - Erkenntnisse für Neubau und Erhaltung. Bauingenieur **77**(12), 559–567 (2002)
8. Küttenbaum, S., Braml, T., Taffe, A., Keßler, S., Maack, S.: Reliability assessment of existing structures using results of nondestructive testing. Struct. Concr. **22**(5), 2895–2915 (2021). https://doi.org/10.1002/suco.202100226
9. Shevaldykin, V.G., Samokrutov, A.A., Kozlov, V.N.: Ultrasonic Low-Frequency Short-Pulse Transducers with Dry Point Contact: Development and Application. Proceedings of International Symposium, NDT-CE, Berlin, Germany (2003)
10. Shull, P.J. (ed.): Nondestructive Evaluation: Theory, Techniques and Applications. Dekker, M., New York (2002). https://doi.org/10.1201/9780203911068
11. Knödel, K., Krummel, H., Lange, G. (eds.): Handbuch zur Erkundung des Untergrundes Von Deponien: Band 3: Geophysik. Springer, Berlin, Germany (2005)
12. Mielentz, F., Feller, V., Krause, M., Orglmeister, R.: Ultraschallprüfung von betonbauteilen-laufzeitgesteuerte gruppenstrahler mit punktkontaktprüfköpfen. Mater. Test. **57**(4), 329–336 (2015)
13. Krautkrämer, J., Krautkrämer, H.: Werkstoffprüfung Mit Ultraschall. Springer, Heidelberg (1986). https://doi.org/10.1007/978-3-662-10909-0
14. Unterausschuss Ultraschallprüfung FA ZfP im Bauwesen: Merkblatt B 04 Ultraschallverfahren zur Zerstörungsfreien Prüfung im Bauwesen. Deutsche Gesellschaft für Zerstörungsfreie Prüfung DGZfP (2018)
15. Holmes, C., Drinkwater, B.W., Wilcox, P.D.: Post-processing of the full matrix of ultrasonic transmit-receive array data for non-destructive evaluation. NDT & e Int. **38**(8), 701–711 (2005). https://doi.org/10.1016/j.ndteint.2005.04.002

16. Kuchipudi, S.T., Ghosh, D.: An ultrasonic wave-based framework for imaging internal cracks in concrete. Struct. Control. Health Monit. **29**(12), 3108 (2022). https://doi.org/10.1002/stc.3108
17. Buske, S.: Three-dimensional pre-stack kirchhoff migration of deep seismic reflection data. Geophys. J. Int. **137**(1), 243–260 (1999)
18. Schickert, M., Krause, M., Müller, W.: Ultrasonic imaging of concrete elements using reconstruction by synthetic aperture focusing technique. J. Mater. Civ. Eng. **15**, 235–246 (2003). https://doi.org/10.1061/(ASCE)0899-1561(2003)15:3(235)
19. Mayer, K., Marklein, R., Langenberg, K.-J., Kreutter, T.: Three-dimensional imaging system based on Fourier transform synthetic aperture focusing technique. Ultrasonics **28**(4), 241–255 (1990). https://doi.org/10.1016/0041-624X(90)90091-2
20. Mayer, K., Langenberg, K.-J., Krause, M., Milmann, B., Mielentz, F.: Characterization of reflector types by phase-sensitive ultrasonic data processing and imaging. J. Nondestr. Eval. **27**(1), 35–45 (2008). https://doi.org/10.1007/s10921-008-0035-3
21. Choi, H., Bittner, J., Popovics, J.S.: Comparison of ultrasonic imaging techniques for full-scale reinforced concrete. Transp. Res. Rec. **2592**(1), 126–135 (2016). https://doi.org/10.3141/2592-14
22. Hoegh, K., Khazanovich, L.: Extended synthetic aperture focusing technique for ultrasonic imaging of concrete. NDT & E Int. **74**, 33–42 (2015). https://doi.org/10.1016/j.ndteint.2015.05.001
23. Shokouhi, P., Wolf, J., Wiggenhauser, H.: Detection of delamination in concrete bridge decks by joint amplitude and phase analysis of ultrasonic array measurements. J. Bridg. Eng. **19**(3), 04013005 (2014). https://doi.org/10.1061/(ASCE)BE.1943-5592.0000513
24. Lay, V., Effner, U., Niederleithinger, E., Arendt, J., Hofmann, M., Kudla, W.: Ultrasonic quality assurance at magnesia shotcrete sealing structures. Sensors **22**(22), 8717 (2022). https://doi.org/10.3390/s22228717
25. Ghosh, D., Kumar, R., Ganguli, A., Mukherjee, A.: Nondestructive evaluation of rebar corrosion-induced damage in concrete through ultrasonic imaging. J. Mater. Civ. Eng. **32**(10), 04020294 (2020). https://doi.org/10.1061/(ASCE)MT.1943-5533.0003398
26. Beniwal, S., Ganguli, A.: Localized condition monitoring around rebars using focused ultrasonic field and SAFT. Res. Nondestr. Eval. **27**(1), 48–67 (2016)
27. Effner, U., Mielentz, F., Niederleithinger, E., Friedrich, C., Mauke, R., Mayer, K.: Testing repository engineered barrier systems for cracks-a challenge. Materialwiss. Werkstofftech. **52**(1), 19–31 (2021). https://doi.org/10.1002/mawe.202000118
28. Friese, M., Wiggenhauser, H.: New NDT technique for concrete structures: ultrasonic linear array and advanced imaging techniques. Proceedings of NDE/NDT for Highways and Bridges, Structural Materials Technology (SMT), Oakland (2008)
29. Krause, M., Milmann, B., Mielentz, F., Streicher, D., Redmer, B., Mayer, K., Langenberg, K.-J., Schickert, M.: Ultrasonic imaging methods for investigation of post-tensioned concrete structures: a study of interfaces at artificial grouting faults and its verification. J. Nondestr. Eval. **27**, 67–82 (2008). https://doi.org/10.1007/s10921-008-0033-5
30. Ballier, G., Mayer, K., Langenberg, K.-J., Schulze, S., Krause, M.: Improvements on Tendon Duct Examination by Modelling and Imaging with Synthetic Aperture and One-Way Inverse Methods. Proceedings of 18th world conference on nondestructive testing, Durban, South Africa (2012)
31. McMechan, G.A.: Migration by extrapolation of time-dependent boundary values. Geophys. Prospect. **31**(3), 413–420 (1983). https://doi.org/10.1111/j.1365-2478.1983.tb01060.x
32. Baysal, E., Kosloff, D.D., Sherwood, J.W.C.: Reverse time migration. Geophysics **48**(11), 1514–1524 (1983). https://doi.org/10.1190/1.1441434
33. Zhou, H., Hu, H., Zou, Z., Wo, Y., Youn, O.: Reverse time migration: a prospect of seismic imaging methodology. Earth Sci. Rev. **179**, 207–227 (2018). https://doi.org/10.1016/j.earscirev.2018.02.008
34. Farmer, P.A., Jones, I.F., Zhou, H., Bloor, R.I., Goodwin, M.C.: Application of reverse time migration to complex imaging problems. First Break **24**(9), 65–73 (2006). https://doi.org/10.3997/1365-2397.24.9.27105
35. Ding, Y., Malehmir, A.: Reverse time migration (RTM) imaging of iron oxide deposits in the Ludvika mining area. Sweden. Solid Earth **12**(8), 1707–1718 (2021). https://doi.org/10.5194/se-12-1707-2021
36. Chang, J., Wang, C., Tang, Y., Li, W.: Numerical investigations of ultrasonic reverse time migration for complex cracks near the surface. IEEE Access **10**, 5559–5567 (2022). https://doi.org/10.1109/ACCESS.2021.3140119
37. Zhang, Y., Gao, X., Zhang, J., Jiao, J.: An ultrasonic reverse time migration imaging method based on higher-order singular value decomposition. Sensors **22**(7), 2534 (2022). https://doi.org/10.3390/s22072534
38. Müller, S., Niederleithinger, E., Bohlen, T.: Reverse time migration: a seismic imaging technique applied to synthetic ultrasonic data. Int. J. Geophys. (2012). https://doi.org/10.1155/2012/128465
39. Hu, M., Chen, S., Pan, D.: Reverse time migration based ultrasonic wave detection for concrete structures. Proceedings of design, construction and maintenance of bridges: Geo-Hubei international conference on sustainable infrastructure, pp. 53-60 (2014)
40. Liu, H., Xia, H., Zhuang, M., Long, Z., Liu, C., Cui, J., Xu, B., Hu, Q., Liu, Q.: Reverse time migration of acoustic waves for imaging based defects detection for concrete and CFST structures. Mech. Syst. Signal Process. **117**, 210–220 (2019). https://doi.org/10.1016/j.ymssp.2018.07.011
41. Qi, Y., Chen, Z., Liu, H., Qi, Y., Tong, H., Xie, J.: Ultrasonic inspection of prefabricated constructions using reverse time migration imaging method. In: 2019 IEEE international conference on signal, information and data processing (ICSIDP), pp. 1–4 (2019). https://doi.org/10.1109/ICSIDP47821.2019.9172817
42. Grohmann, M., Niederleithinger, E., Buske, S.: Geometry determination of a foundation slab using the ultrasonic echo technique and geophysical migration methods. J. Nondestruct. Eval. (2016). https://doi.org/10.1007/s10921-016-0334-z
43. Grohmann, M., Müller, S., Niederleithinger, E., Sieber, S.: Reverse time migration: introducing a new imaging technique for ultrasonic measurements in civil engineering. Near Surf. Geophys. **15**(3), 242–258 (2017). https://doi.org/10.3997/1873-0604.2017006
44. Chen, T., Huang, L.: Imaging Faults Using Elastic Reverse-Time Migration With Updated Velocities of Waveform Inversion. GRC Trans. **37**, 999–1003 (2013)
45. Rocha, D., Sava, P.: Elastic least-squares reverse time migration using the energy norm. Geophysics **83**(3), 237–248 (2018). https://doi.org/10.1190/geo2017-0465.1
46. Yan, H., Yang, L., Dai, H., Li, X.-Y.: Implementation of elastic prestack reverse-time migration using an efficient dinite-difference scheme. Acta Geophys. **64**(5), 1605–1625 (2016). https://doi.org/10.1515/acgeo-2016-0078
47. Zhong, Y., Gu, H., Liu, Y., Mao, Q.: Elastic reverse-time migration with complex topography. Energies (2021). https://doi.org/10.3390/en14237837
48. Xiao, X., Leaney, W.S.: Local vertical seismic profiling (VSP) elastic reverse-time migration and migration resolution: salt-flank imaging with transmitted P-to-S waves. Geophysics **75**(2), 35–49 (2010). https://doi.org/10.1190/1.3309460
49. Shi, Y., Zhang, W., Wang, Y.: Seismic elastic RTM with vector-wavefield decomposition. J. Geophys. Eng. **16**(3), 509–524 (2019). https://doi.org/10.1093/jge/gxz023
50. Jing, C., Singh, V.P., Custodio, D., Cha, Y.H., Ross, W.S.: Benefits and Applications of Elastic Reverse Time Migration in Salt-related Imaging. Expanded abstract, society of exploration geophysicists

international exposition and 87th annual meeting, 2017 (2017). https://doi.org/10.1190/segam2017-17409572.1
51. Grohmann, M., Niederleithinger, E., Buske, S., Büttner, C.: Application of elastic P-SV reverse time migration to synthetic ultrasonic echo data from concrete members. J. Nondestr. Eval. (2023). https://doi.org/10.1007/s10921-023-00962-w
52. Anderson, B.E., Griffa, M., Bas, P.-Y.L., Ulrich, T.J., Johnson, P.A.: Experimental implementation of reverse time migration for nondestructive evaluation applications. J. Acoust. Soc. Am. **129**(1), 8–14 (2011). https://doi.org/10.1121/1.3526379
53. Rao, J., Yang, J., He, J., Huang, M., Rank, E.: Elastic least-squares reverse-time migration with density variation for flaw imaging in heterogeneous structures. Smart Mater. Struct. **29**(3), 035017 (2020). https://doi.org/10.1088/1361-665X/ab6ba4
54. Mizota, H., Amano, Y., Nakahata, K.: Application of the reverse time migration method to ultrasonic nondestructive imaging for anisotropic materials. Mater. Eval. **80**(7), 28–37 (2022). https://doi.org/10.32548/2022.me-04244
55. Nguyen, L.T., Kocur, G.K., Saenger, E.H.: Defect mapping in pipes by ultrasonic wavefield cross-correlation: a synthetic verification. Ultrasonics **90**, 153–165 (2018). https://doi.org/10.1016/j.ultras.2018.06.014
56. Beniwal, S., Ganguli, A.: Defect detection around rebars in concrete using focused ultrasound and reverse time migration. Ultrasonics **62**, 112–125 (2015). https://doi.org/10.1016/j.ultras.2015.05.008
57. Nguyen, L.T., Modrak, R.T.: Ultrasonic wavefield inversion and migration in complex heterogeneous structures: 2d numerical imaging and nondestructive testing experiments. Ultrasonics **82**, 357–370 (2018). https://doi.org/10.1016/j.ultras.2017.09.011
58. Liu, H., Qi, Y., Chen, Z., Tong, H., Liu, C., Zhuang, M.: Ultrasonic inspection of grouted splice sleeves in precast concrete structures using elastic reverse time migration method. Mech. Syst. Signal Process. **148**, 107152 (2021). https://doi.org/10.1016/j.ymssp.2020.107152
59. Asadollahi, A., Khazanovich, L.: Analytical reverse time migration: an innovation in imaging of infrastructures using ultrasonic shear waves. Ultrasonics **88**, 185–192 (2018). https://doi.org/10.1016/j.ultras.2018.04.005
60. Asadollahi, A., Khazanovich, L.: Analytical reverse time migration with new imaging conditions for one-sided nondestructive evaluation of concrete elements using shear waves. Ultrasonics **99**, 105960 (2019). https://doi.org/10.1016/j.ultras.2019.105960
61. Büttner, C., Niederleithinger, E., Buske, S., Friedrich, C.: Ultrasonic echo localization using seismic migration techniques in engineered barriers for nuclear waste storage. J. Nondestr. Eval. **40**(4), 1–10 (2021). https://doi.org/10.1007/s10921-021-00824-3
62. Sava, P., Hill, S.J.: Overview and classification of wavefield seismic imaging methods. Lead. Edge **28**(2), 170–183 (2009). https://doi.org/10.1190/1.3086052
63. Liu, F., Zhang, G., Morton, S.A., Leveille, J.P.: An effective imaging condition for reverse-time migration using wavefield decomposition. Geophysics **76**(1), 29–39 (2011). https://doi.org/10.1190/1.3533914
64. Kaelin, B., Guitton, A.: Imaging condition for reverse time migration. Seg Technical Program Expanded Abstracts. Society of Exploration Geophysicists, 2594-2598 (2006)
65. Fomel, S., Sava, P., Vlad, I., Liu, Bashkardin, V.: Madagascar: open source software project for multidimensional data analysis and reproducible computational experiments. J. Open Res. Softw. (2013). https://doi.org/10.5334/jors.ag
66. Reinhardt, H.W.: Zerstörungsfreie Strukturbestimmung von Betonbauteilen mit akustischen und elektromagnetischen Echo-Verfahren: Abschlussbericht Forschergruppe FOR384. Liste der erstellten Prüfkörper, Anhang (2007)
67. Bohlen, T., Saenger, E.H.: Accuracy of heterogeneous staggered-grid finite-difference modeling of Rayleigh waves. Geophysics **71**(4), 109–115 (2006). https://doi.org/10.1190/1.2213051
68. Clayton, R., Engquist, B.: Absorbing boundary conditions for acoustic and elastic wave equations. Bull. Seismol. Soc. Am. **67**(6), 1529–1540 (1977). https://doi.org/10.1785/BSSA0670061529
69. Cerjan, C., Kosloff, D., Kosloff, R., Reshef, M.: A nonreflecting boundary condition for discrete acoustic and elastic wave equations. Geophysics **50**(4), 705–708 (1985). https://doi.org/10.1190/1.1441945
70. Jiang, Z.: Elastic wave modelling and reverse-time migration by a staggered-grid finite-difference method Doctoral thesis, University of Calgary, Calgary, Canada (2012). https://doi.org/10.11575/PRISM/25850
71. Gholamy, A., Kreinovich, V.: Why Ricker wavelets are successful in processing seismic data: towards a theoretical explanation. Paper presentet at IEEE symposium on computational intelligence for engineering solutions (CIES), Orlando Florida, USA (2014). https://doi.org/10.1109/CIES.2014.7011824
72. Ricker, N.: The form and laws of propagation of seismic wavelets. Geophysics (1953). https://doi.org/10.1190/1.1437843
73. Saenger, E.H., Gold, N., Shapiro, S.A.: Modeling the propagation of elastic waves using a modified finite-difference grid. Wave Motion **31**(1), 77–92 (2000). https://doi.org/10.1016/S0165-2125(99)00023-2
74. Maack, S.: Untersuchungen zum schallfeld niederfrequenter ultraschallprüfköpfe für die anwendung im bauwesen. PhD thesis, Bundesanstalt für Materialforschung und-prüfung (BAM) (2012)
75. Sridhar, S.: Digital Image Processing. Oxford University Press, India (2011)
76. Mayer, K., Cinta, P.M.: User Guide of Graphical User Interface inter_saft. Department of Computational Electronics and Photonics, University of Kassel (2012)
77. Geoltrain, S., Brac, J.: Can we image complex structures with first-arrival traveltime? Geophysics **58**(4), 564–575 (1993). https://doi.org/10.1190/1.1443439